Electrochemical and Tribological Behavior of Ni-Co/ZrO$_2$ Coatings Prepared by Ultrasound-Assisted Electrodeposition

Yiyong Wang[*], *Zhipeng Liang, Xinyu Zhou, Hui Jin*

College of Material and Metallurgy, University of Science and Technology Liaoning, Anshan 114051, China;
[*]E-mail: <u>wangyiyongfly@163.com</u>

Ni-Co composite coatings reinforced with ZrO$_2$ were obtained by ultrasound-assisted electrodeposition. The electrodeposition kinetics were investigated using linear sweep and cyclic voltammetry. The morphology and coating phases of the coatings were characterized by scanning electron microscopy and X-ray diffraction, respectively. Results indicated that the electrocrystallization of Co^{2+} was controlled by a three-dimensional "nucleation/growth" process. The initial co-deposition potentials of the alloy and composite coatings were −0.72 V vs. SCE and −0.70 V vs. SCE, respectively. During co-deposition, ZrO$_2$ restrained the discharge of H$^+$ and reduced the cathodic polarization. When the amount of added ZrO$_2$ was 10 g L^{-1}, the nanohardness, anti-corrosion and wear resistance of the Ni-Co/ZrO$_2$ composite were evidently improved compared with the Ni-Co alloy. The average nanohardness of the Ni-Co/ZrO$_2$ composite was 6.13 GPa, which was approximately 1.5 times higher than that of the Ni-Co alloy (4.12 GPa). After 40 min of rotational wear testing, the wear loss of the Ni-Co alloy was approximately twice compare with the Ni-Co/ZrO$_2$ composite. The high hardness and low defect density in the composite coatings reduced the plastic deformation and adhesive wear of the Cu substrates, leading to a significant improvement wear properties.

1. INTRODUCTION

Composite electrochemical coatings containing embedded second phase particles exhibit improved wear resistance, self-lubrication and corrosion resistances. Hard particles such as Al$_2$O$_3$ [1], TiN [2] and ZrO$_2$ [3] have been successfully incorporated into metallic coatings using Watts and sulfamate baths. When incorporated in a metal matrix, the particles enhance the properties of the surfaces (e.g., hardness, wear and corrosion resistance) and confer new properties (e.g., antifriction and magnetic)

on them. Fine ceramic nanoscale particles are frequently used to achieve high hardness and strength in ceramic-reinforced metal matrix composites (MMCs) via a dispersion hardening mechanism [4]. However, agglomeration of nanoparticles in both the electrolyte and coatings restrict the further application of MMCs. Therefore, it remains a great challenge to achieve a well-dispersed and concentrated particle distribution throughout MMCs by electrodeposition. It is currently accepted that anionic or cationic surfactants are the most effective dispersants for preventing particle agglomeration in both electrolytes and coatings. Typical surfactants include sodium dodecyl sulfate (SDS), hexadecylpyridinium bromide (HPB) and cetyltrimethylammonium bromide (CTAB) [5]. However, the use of surfactants may exert an influence on the process control, effluent disposal and lifespan of the electrolytes in electroplating industry. Based on these reasons, other options to replace surfactant use are being evaluated [6].

When ultrasound is introduced during the deposition process, its cavitation effect can effectively prevent the agglomeration of particles and induce uniform dispersion and continuous suspension [7]. Ultrasound-assisted electrodeposition has therefore attracted significant attention in recent years. Ignacio Tudela [8] reported ultrasound-assisted electrodeposited Ni-hBN and Ni-WS$_2$ composite coatings on Cu without a surfactant, and these Nickel-based composite coatings with second phase particles were shown to contain uniformly distributed particles. García-Lecina [9] prepared the Ni composite coatings with WS$_2$ nanoparticles by electrochemical deposition under ultrasound, it is the best example to illustrate that the ultrasound can significantly improve particle dispersion and content, coating structure and compactness, achieving better mechanical properties.

Although the ultrasound has been successfully applied to in the electrodeposition of MMCs, not only on the basis of improving the dispersion of particles in electroplate liquid but also in enhancing the incorporation of well-dispersed particles into coatings, the mechanism of ultrasound-assisted co-deposition remains unclear. In this study, Ni-Co/ZrO$_2$ composite coatings were prepared by ultrasound-assisted electrodeposition in an aminosulfonate bath. The electrochemical behavior of nanoparticles in the composite deposition process and the co-deposition of alloy and nanoparticles were investigated by electrochemical methods including linear sweep voltammetry (LSV), cyclic voltammetry (CV) and electrochemical impedance spectroscopy (EIS). Simultaneously, the effect of nano-sized ZrO$_2$ on the microstructure, corrosion resistance and tribological properties of Ni-Co/ZrO$_2$ composite coatings was investigated in detail.
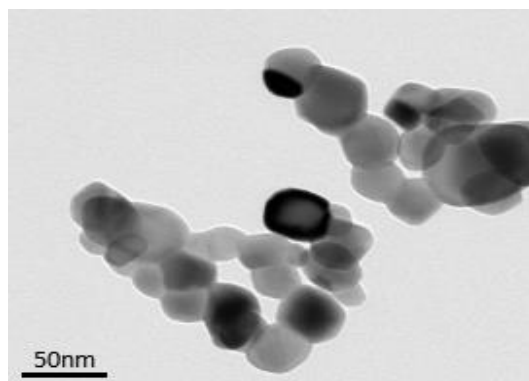
2. EXPERIMENTAL AND METHODS

2.1 Materials

Copper sheets with dimensions of 25×25 cm^2 were used as cathodes. The substrates were degreased in the methanol and activated in 10 wt% HCl solution before rinsing with distilled water. The electrodeposition bath was a standard sulfamate solution. Analytical reagent grade chemicals were added to distilled water to form the electrolyte solution. The composition and treatment method of different plating bath are shown in Table 1. Nanoparticulate ZrO$_2$ (Fig. 1) with an average particle size of 50 nm and purity above 99.99% was used in the coatings. The electrodeposition parameters are shown as

follows: solution temperature 53–55°C, current density 2.5 A dm^{-2}, pH 4.0–4.2 and stirring speed 500 rpm. A 600 mL beaker containing 500 mL of the sulfamate bath with ZrO$_2$ particles was immersed in a QS12 ultrasonic bath (Ultrawave Ltd). This was equipped with a built-in thermostat, enabling temperature control up to 70°C, and was operated at a frequency of around 35 kHz with an ultrasonic power of 240 W. And Table 2 presents the parameter of nanoparticle concentrations for various electrodeposited Ni-Co alloy and Ni-Co/ZrO$_2$ composite coatings.

Table 1. Composition and treatment methods of different plating baths.

Samples	Solution	Composition (g L^{-1})				Treatment(W)
		Ni(NH$_2$SO$_3$)$_2$·4H$_2$O	Co(NH$_2$SO$_3$)$_2$·4H$_2$O	H$_3$BO$_3$	ZrO$_2$	Ultrasound
Sol.-a	blank	-	-	50	-	-
Sol.-b	Ni	80	-	50	-	-
Sol.-c	Co	-	12	50	-	-
Sol.-d	Ni-Co	80	12	50	-	-
Sol.-e	Ni-Co/ZrO$_2$	80	12	50	5	-
Sol.-f	Ni-Co/ZrO$_2$	80	12	50	5	240

Figure 1. The transmission electron microscopy (TEM) image of the used ZrO$_2$ powder

Table 2. Ni-Co alloy and Ni-Co/ZrO$_2$ composite coatings prepared under various nanoparticle concentrations.

Samples	Coating	ZrO$_2$ concentration (g L^{-1})	Ultrasonic power (W)
Coating-I	Ni-Co	0	240
Coating-II	Ni-Co/ZrO$_2$	5	240
Coating-III	Ni-Co/ZrO$_2$	10	240

2.2 Methods

The electrochemical tests were carried out by the use of a conventional single-compartment glass three-electrode cell with 25-mL capacity. A saturated calomel reference electrode, and a platinum counter electrode were employed for measurements. The prepared coatings were used as working electrode, especially, the exposed area of the tested coatings is 1.0 cm^2 for corrosion test. Cathodic scans

were performed by ramping the potential from 0 to -1.5 V at a scan rate of 20 mVs^{-1}. CV experiments were initiated at 0 V vs. SCE in the negative direction, reversing at switching potentials (0.5 V) to the positive direction at a scan rate (SR) of 20 mVs^{-1}. EIS experiments were performed at frequencies of 10^{-1} to 10^5 Hz at a deposition potential of -1.1 V. Electrochemical corrosion tests on the coatings were performed in 3.5 wt% NaCl solution. Potentiodynamic polarization measurements were recorded within the potential scanning range of -1.0 V to $+0.5$ V at a scan rate of 1 mVs^{-1} for corrosion characterization. The value of corrosion potential (E_{corr}) and corrosion current density (i_{corr}) were determined based on the Tafel extrapolation. An AUTOLAB electrochemical workstation (Metrohm, Switzerland) was used for LSV, CV, EIS and corrosion tests.

X-ray diffraction (X˙ Pert Powder) was employed for evaluate the phase composition and average grain size of the samples (Cu Kα filtered radiation). Structural characterization of the coatings was performed via SEM (Zeiss-ΣIGMA HD). Transmission electron microscopy (TEM, JEM-2100) was used to analyze the morphology of nanoparticulate ZrO$_2$. The chemical composition of the samples was performed by energy dispersive spectroscopy (EDS) in SEM using an OXFORD-X-Max 50-mm^2 spectrometer. The nanohardness and Young's modulus were measured during an indentation test with a Vickers diamond indenter according to standard ISO 14577-1 (Nanoindenter G200, KEYSIGHT Instruments). The HX-1000TM/LCD microhardness tester is used to measure the Vickers microhardness (HV) of deposits under a 200 g load for 10 s, and the final microhardness is the average of 10 measurements. The wear properties of the coatings were determined by the use of a ball-on-disc device. In the test, the corundum ball with 1-cm-diameter is the counter body. The test parameters: 5- mm-diameter wear track, 200 rpm rotation speed, a normal load of 4 N, and a total of 8,000 cycles. After the wear test, the mass loss of coatings was measured by a microbalance with the accuracy of $\pm\, 0.1\mu$g.

3. RESULTS AND DISCUSSION

3.1. Electrochemical behavior

Fig. 2 shows the LSV curves of Ni^{2+}, Co^{2+}, Ni^{2+}-Co^{2+} and Ni^{2+}-Co^{2+}/ZrO$_2$ reduction processes. As seen in Fig. 2a, there were no reduction reactions in the base bath except for the reduction of Ni and Co, which shows that the base plating solution is relatively chemically stable. As seen for the whole examined polarization range, the Co deposition curve lay at more negative potentials in relation to that of the individual Ni discharge, corresponding to a higher current density. This indicates that Co is more difficult to reduce than Ni in this type of deposition system. The Ni-Co deposition curve is shifted in between those of the Ni and Co discharges. The deposition curve was closer to Ni, showing that the deposition of Co is underpotential deposition (UPD) and is promoted by the Ni in the alloy bath. A turning point can be seen in the Ni deposition curve at a potential of -0.74 V (Fig. 2a), illustrating that reduction of Ni^{2+} was initiated and that the current density increased as the scanning potential is increased. In the Co deposition curve, reduction of Co^{2+} began at a potential of -0.80 V. As shown in the diagram, the deposition potential of the alloy was -0.73 V, which was obscured by the deposition potential of Ni and Co and was closer to that of Ni. Furthermore, the addition of Ni promoted the discharge reduction of Co.
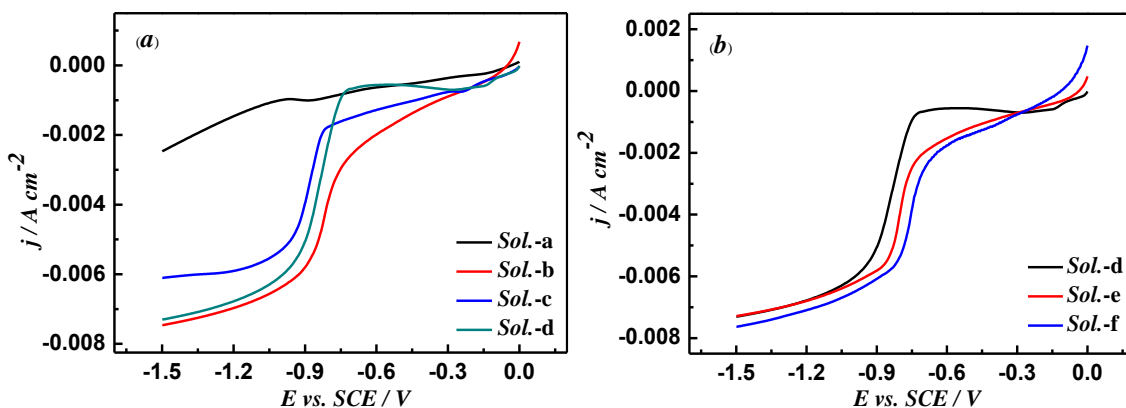
Figure 2. Cathodic polarization curves for copper electrode in (a): a-blank, b-Ni, c-Co and d-Ni-Co; (b): d-Ni-Co, e-Ni-Co/ZrO$_2$ (5 g L^{-1}) and f-Ni-Co/ZrO$_2$ (10 g L^{-1}) electroplating bath solutions. T=55℃, pH=4.0, SR=20 mVs^{-1}.

As shown in the Fig. 2b, the addition of ZrO$_2$ to the electrolyte shifted the deposition potential in the positive direction and decreased the cathodic polarization to facilitate the electrode process. As observed for the entire examined polarization range, the initial stage of the curve exhibited no diffusion-controlled peak, and the deposition current did not reach the limiting diffusion current, indicating that the cathode deposition process is not governed by mass transfer. It is reported that SiC [10] particles in the nickel plating solution are reported to adsorb Ni^{2+} and make the surface positively charged, and CeO$_2$ [11] powder also adsorbs metal ions from the solution. Thus, the surfaces of ZrO$_2$ particles in the plating solution may also adsorb Ni^{2+} and Co^{2+} ions and become positively charged, and the metal ions adsorbed by the particles reduce due to the constant collision of particles with the cathode plate. The addition of ZrO$_2$ particles to the bath caused the reduction of these metal ions, leading to a lower degree of polarization of the system. Ultrasound strengthened the role of nanoparticles, further shifting the deposition potential in the positive direction, showing that ultrasound effectively reduces the agglomeration of nanoparticles in the bath and promotes dispersion, creating a uniform and stable bath.

According to previous studies[12], the reduction in Me^{2+} during electrodeposition is usually a multistep reaction. Generally, in the cathode reaction, Me$^+$ is adsorbed on the electrode surface for reduction. During electrodeposition, the concentration of localized hydrogen ions will increase near the cathode surface, resulting in hydroxide formation. The chemical reaction paths for Me^{2+} reduction in acidic medium can be expressed as follows:

$$Me^{2+} + H_2O \rightarrow Me(OH)^{2+} + H^+ \qquad (1)$$

$$(MeOH^{2+}) + e^- \rightarrow (MeOH)_{ads} \qquad (2)$$

$$Me(OH)_{ads} + e^- \rightarrow Me + OH^- \qquad (3)$$

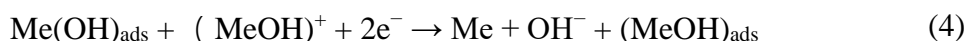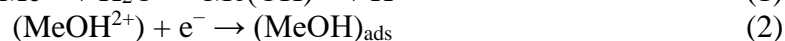$$Me(OH)_{ads} + (MeOH)^+ + 2e^- \rightarrow Me + OH^- + (MeOH)_{ads} \qquad (4)$$

Fig. 3a shows CV tests of Ni and Co, and (b) shows CV tests of the co-deposition of Ni-Co in bath solutions with and without ZrO$_2$. As shown in Fig. 3a, the deposition potentials of Ni and Co are consistent with those obtained by polarization curves. For the CV curve of Ni, oxidation peak A, for which the potential is −0.26 V, appears on the curve for the positive scan, corresponding to the oxide precipitation of deposited nickel. However, the CV curve of Co shows no oxidation peak, indicating that

Ni is more easily oxidized than Co, and that Co has strong corrosion resistance in this system. In the Co curve, a current loop appears on the curve at the end of the scan, indicating that the electrodeposition behavior of Co^{2+} follows the 3D "nucleation/growth" mechanism [13].

Fig. 3b shows the voltammograms of Ni-Co co-deposition, in which reduction peak A is located at −0.27 V in the negative scan, corresponding to hydrogen reduction and the possible reduction reactions for the hydrogen evolution reactions (HER) [14], which are obtained from Eqs. (5) and (6).

$$H_3O^+ + 2e^- \rightarrow H_2OH^- \tag{5}$$
$$2H_2O + 2e^- \rightarrow H_2 + OH \tag{6}$$

However, the cyclic voltammetry curves of Ni-Co/ZrO$_2$ contained no hydrogen evolution peak, indicating that the addition of nanoparticles and ultrasound effectively inhibited the hydrogen evolution reaction. The added nanoparticles spread rapidly in the plating solution, and those adsorbed on the cathode plate occupied many active sites, thereby suppressing the hydrogen evolution reaction, and the ultrasonic cavitation effect produced by acoustic streaming, microinjection and shock waves effectively reduced the agglomeration of nanoparticles, thereby promoting adsorption. Reduction peak B corresponds to the co-deposition of Ni-Co, deposition occurred at a potential of −0.73 V in the alloy plating solution and at −0.70 V in the composite plating solution, indicating that the presence of nanoparticles decreased the deposition potential. This was because of the adsorption of nanoparticles on the electrode, the adsorbed ion layer that formed around the particles accelerated the migration of ions to the cathode, increasing the active area of the cathode surface and resulting in a positive shift in the deposition potential [15]. When the scan direction was changed, the oxidation peak appeared at C and D, corresponding to the oxidation precipitation of the deposited alloy and copper matrix.
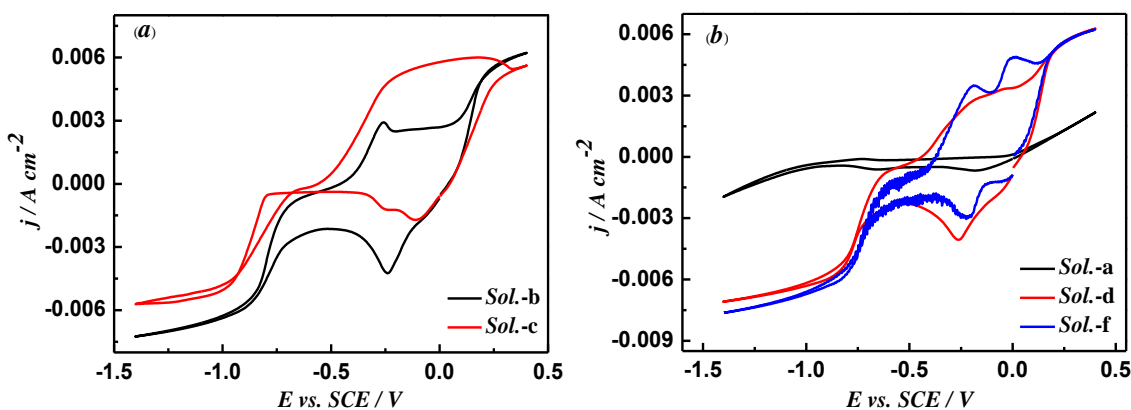
Figure 3. CV test on copper electrode in (a): b-Ni and c-Co; (b): a-blank, d-Ni-Co and f-Ni-Co/ZrO$_2$ (10 g L^{-1}) electroplating bath solutions. T=55℃, pH=4.0, SR=20 mVs^{-1}.

Fig. 4 shows Nyquist plots of simulated impedance spectra for Ni-Co and Ni-Co/ZrO$_2$ deposition. In all cases, the correlation between experimental and simulated data was acceptable. The equivalent electrical circuit (EC) was determined with the ZVIEW program and is shown in Fig. 4. In the EC, R_c represents the faradaic resistance, R_s represents the solution resistance between the working electrode and the reference electrode, R_{ct} represents the charge transfer resistance and Cdl is a constant phase element which represents the double layer capacitance. The calculated data of the circuit elements is summarized in Table 3.

As shown in Nyquist diagram, there are two loops in the impedance plots of the coatings, including a large, slightly depressed, asymmetric capacitive loop and an inductive loop at high and low frequencies, respectively. The high frequency loop relates to the double layer capacitance in parallel with the charge transfer resistance, whereas the inductive loop is attributed to the adsorption of reaction intermediates. As demonstrated in Table 3, the solution resistance decreased as the concentration of ZrO_2 increased. This indicates that adding ZrO_2 significantly affected the solution resistance between the reference and the working electrodes. The charge transfer resistance of 10 g L^{-1} ZrO_2 co-deposition (R_{ct} = 12.42 Ω cm^2) is lower than Ni-Co electroplating (R_{ct} = 14.25 Ω cm^2). R_{ct} may be directly proportional to the surface diffusion of metal anions on the substrate surface. This could confirm the hypothesis that the ZrO_2 nanoparticles enhanced the ionic deliveries to the cathode surface due to their adsorbed ionic layer. Similar findings were reported for co-deposition of Ni with ZrO_2 [16], SiC [17] and TiO_2 [18] nanoparticles.
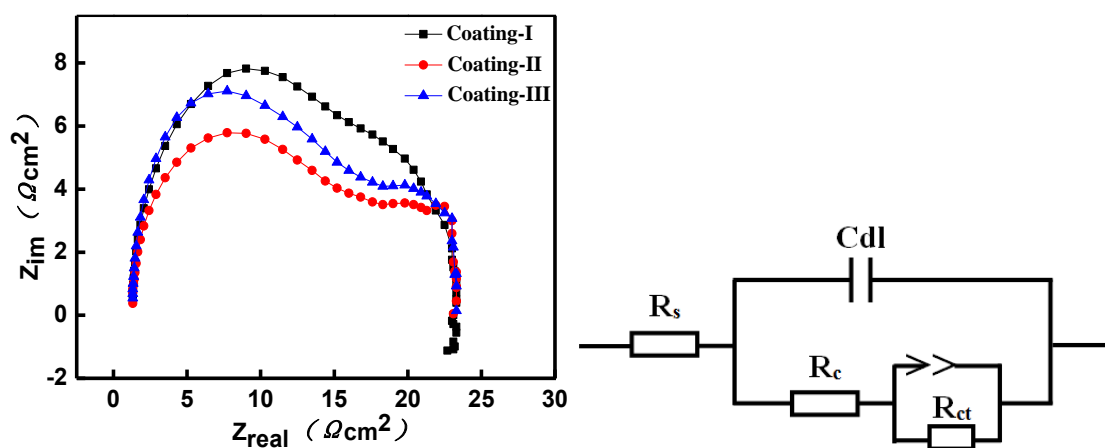
Figure 4. Nyquist plots of experimental and simulated impedance spectra of (I) Ni-Co alloy, (II) Ni-Co/ZrO_2 (5 g L^{-1}) and (III) Ni-Co/ZrO_2 (10 g L^{-1}) composite coatings.

Table 3. EIS parameters extracted from Nyquist plots in Fig 4.

Samples	Rs/Ω cm^2	Cdl/μF cm^2	Rc/Ω cm^2	CPE-T	CPE-P	Rct/Ω cm^2
Coating-I	1.301	4.967	11.692	4.227E-4	0.7478	14.25
Coating-II	1.076	4.421	9.721	3.557E-4	0.6805	13.96
Coating-III	0.976	3.398	9.169	1.563E−4	0.6236	12.42

3.2 Morphology and microstructural characterization

Fig. 5 shows the SEM micrographs of Ni-Co alloy and Ni-Co/ZrO_2 composite coatings. The Ni-Co alloy exhibited the coarse surface with the feature of dissimilar spherical granular (Fig. 5a). However, the composite coatings exhibited different surface morphology compared with the alloy coating. It can be seen that the size of grains decreased as the concentration of ZrO_2 in the plating solution increased. In particular, the sample fabricated with 10 g L^{-1} ZrO_2 in the plating solution (Fig. 5c) was completely compacted with fine grains. Comparing the morphology of the Ni-Co alloy coating deposited without ZrO_2 and those in the present investigation shown in Fig. 5, it can be concluded that increased

incorporation of nanoparticles affects the morphology and grain size of the composite coating. The improvement of surface morphology could be ascribed to the uniform distribution of ZrO_2 trapping in the Ni-Co matrix, which changes the mechanism of co-deposition/electrocrystallization. Therefore, the ultrasound-assisted electrodeposition process and incorporation of ZrO_2 in the Ni-Co matrix refined the crystal size.
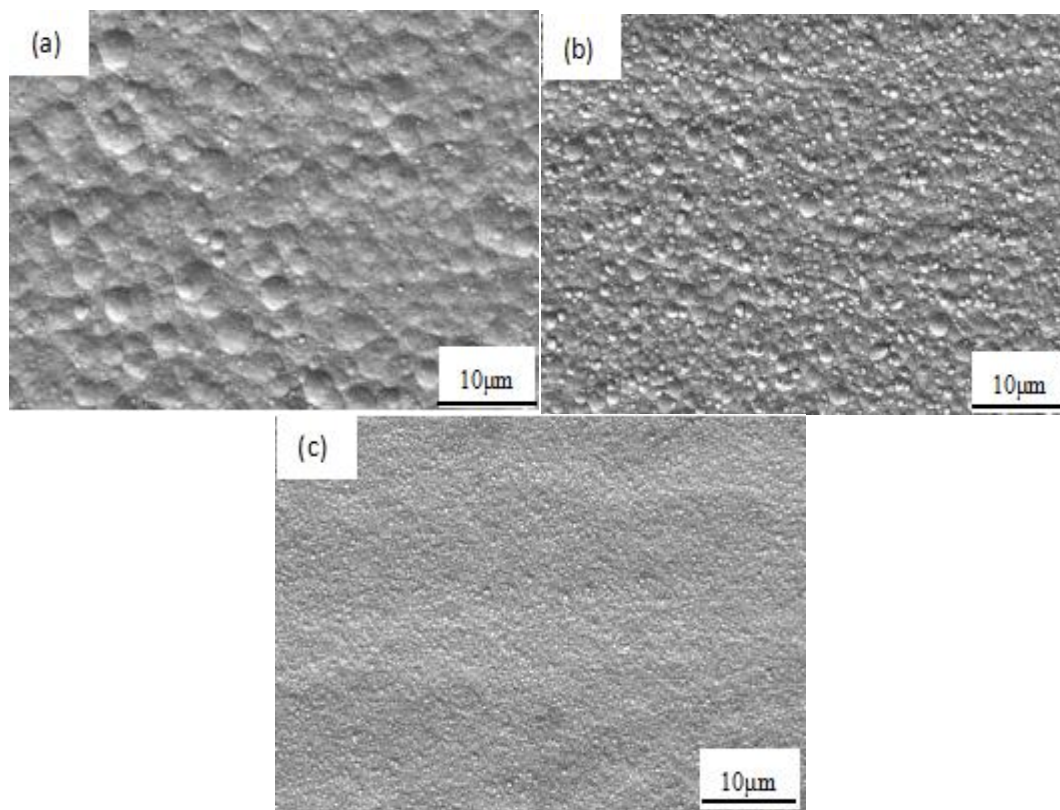
Figure 5. FE-SEM micrographs of the surface of (a) Ni-Co alloy, (b) Ni-Co/ZrO_2 (5 g L^{-1}) and (c) Ni-Co/ZrO_2 (10 g L^{-1}) composite coatings.

Fig. 6 shows the plane scan analysis of the Ni-Co/ZrO_2 composite coating (Coating-III) surface. In Fig. 6c, Zr was uniformly distributed with obvious granularity on the coating surface, which was attributed to ultrasound during electrodeposition causing homogeneous distribution of ZrO_2 in the matrix. Ni, Co and O were distributed uniformly on the coating surface, as shown in Fig. 6a, b and d; the uniform distribution of elements led to the formation of compact coatings and consequently improved their mechanical properties.
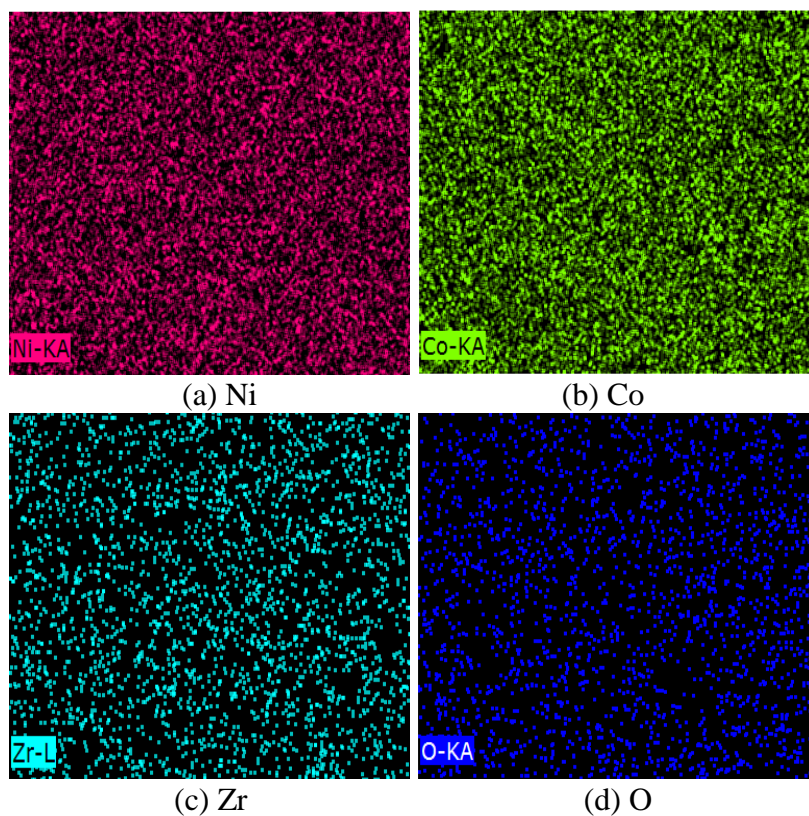
Figure 6. Element EDS mapping of the Ni-Co/ZrO$_2$ (10 g L^{-1}) composite coating.

Fig. 7 presents the cross-sectional images of Ni-Co alloy and Ni-Co/ZrO$_2$ composite coating (Coating-III), which shows the effect of ZrO$_2$ on the thickness and the bond strength between coating and substrate. The coating thickness of Ni-Co was found to be ≈18.37 μm. However, the incorporation of 10 g L^{-1} ZrO$_2$ in the Ni-Co alloy reduced the coating thickness from ≈18.37 to 9.32 μm. This drastic ≈49% decrease in the thickness could be ascribed to the embedded of ZrO$_2$ particles that may form a physical barrier and impede the growth of larger grains (Fig. 7b shows that the growth of the coating proceeds from bottom to top). Swarnima [19] found a similar drift (i.e., 78% reduction) in the coating thickness of electrodeposited Ni-W with the addition of SiC (5 g L^{-1}).
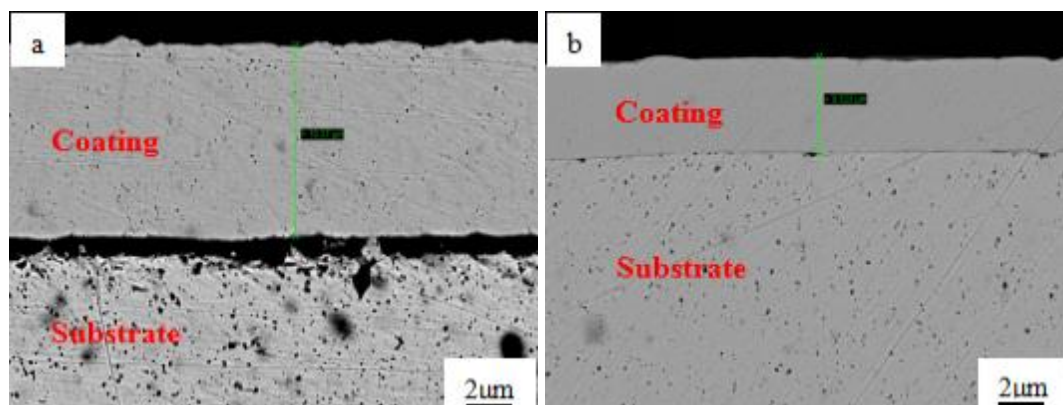
Figure 7. FE-SEM images of the cross-sections of the Ni-Co alloy and Ni-Co/ZrO$_2$ composite coatings: (a) Ni-Co alloy and (b) Ni-Co/ZrO$_2$ (10 g L^{-1}) composite coating.

As shown in Fig. 8a, the grains of the Ni-Co/ZrO$_2$ composite coating (Coating-III) grew perpendicularly from substrate to coating. The Ni-Co/ZrO$_2$ coating interface was analyzed by line scanning.
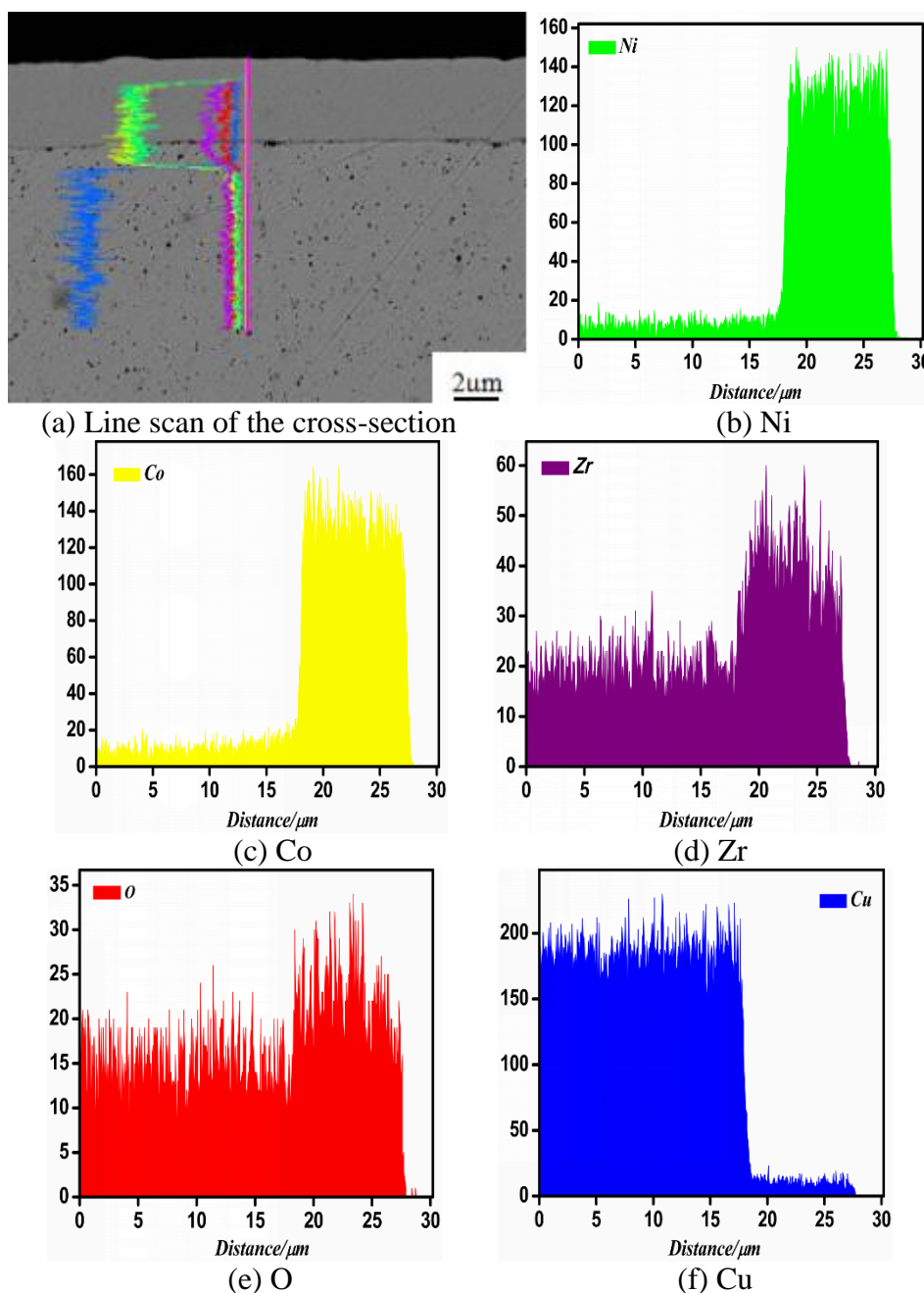

Figure 8. Line scan analysis of the Ni-Co/ZrO$_2$ (10 g L^{-1}) composite coating interface.

Ni and Co element were homogenous distributed with high content in the Ni-Co/ZrO$_2$ composite coating, as shown in Fig. 8b and c. The Zr content increased from the substrate to the surface, and its content in the coating was much higher than in the substrate, as shown in Fig. 8d. The O content was relatively high in the coating, as shown in Fig. 8e. The Cu content in the coating was much higher than in the substrate, as shown in Fig. 8f, and there is a small amount of Cu in the coating because of the atomic diffusion. The content of chemical elements in the coating varied with the gradient, and there is

an obvious interface between the coating and the substrate so that the coating can acquire an appropriate hardness and toughness to effectively inhibit the formation and propagation of cracks and improve its bearing capacity.

Fig. 9 shows the XRD results of the Ni-Co alloy and Ni-Co/ZrO$_2$ composite coatings. The grain size D was calculated by the broadening of the most intense peak (111) using the Scherrer equation (D = 0.9 λ/β cosθ) where λ is the wavelength of the radiation (0.154 nm), β is the full width at half maximum (FWHM) of the peak, and θ is the position of the peak. The grain size of Ni-Co/ZrO$_2$ coatings is smaller than Ni-Co alloy coating. The average grain sizes were found to be 25.9 ± 0.2, 24.9 ± 0.2 and 19.8 ± 0.2 nm for Coating-I, Coating-II and Coating-III, respectively. Grain size is a important factor that determine the mechanical properties of the coatings. Generally, the grain size of a coating is a critical factor to determine its microhardness [20]. According to the well-known Hall–Petch relationship, the microhardness of coatings will increases when the grains are refined. The increase of microhardness of coatings indicated that the incorporation of ZrO$_2$ significantly refines the grains, therefor the Ni-Co/ZrO$_2$ composite coatings exhibited higher microhardness value. Similar the conclusion of structural have been also reported in the case of Ni-Co/TiN composite coating [21].
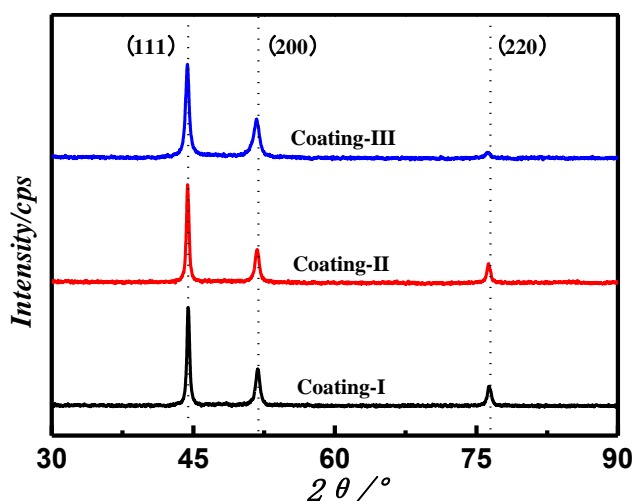

Figure 9. X-ray diffraction pattern of (I) Ni-Co alloy, (II) Ni-Co/ZrO$_2$ (5 g L^{-1}) and (III) Ni-Co/ZrO$_2$ (10 g L^{-1}) composite coatings.

3.3 Nanoindentation test

Fig. 10 shows the nanoindentation curves of Ni-Co alloy and Ni-Co/ZrO$_2$ composite coatings. As shown in Fig. 10, the nanoindentation curves of five points in Coating-III were almost overlapping, indicating that the Coating-III exhibits better uniform surface, which further confirms the SEM results. The average load at maximum depth for Ni-Co is 400 mN, that for the Coating-II is about 400 mN, and that for Coating-III is about 450 mN, corresponding to the maximum indentation depth. The required load for coatings increases gradually, indicating an increase in the coating hardness. The hardness. elastic modulus and H/E of the Ni-Co alloy were 4.12 GPa, 207.1 GPa and 0.019, respectively; the

corresponding values for the Coating-II composite coatings were 5.7 GPa, 215.7 GPa and 0.021, respectively; and those for the Coating-III were 6.13 GPa, 291 GPa and 0.026, respectively. The results indicate that the synergistic effects of ultrasound and nanoparticles could refine grain, increase the grain boundary volume and cohesion, and enhance the resistance to external deformation, thereby improving the mechanical properties of the coating, which are agrees well with other literatures [22].
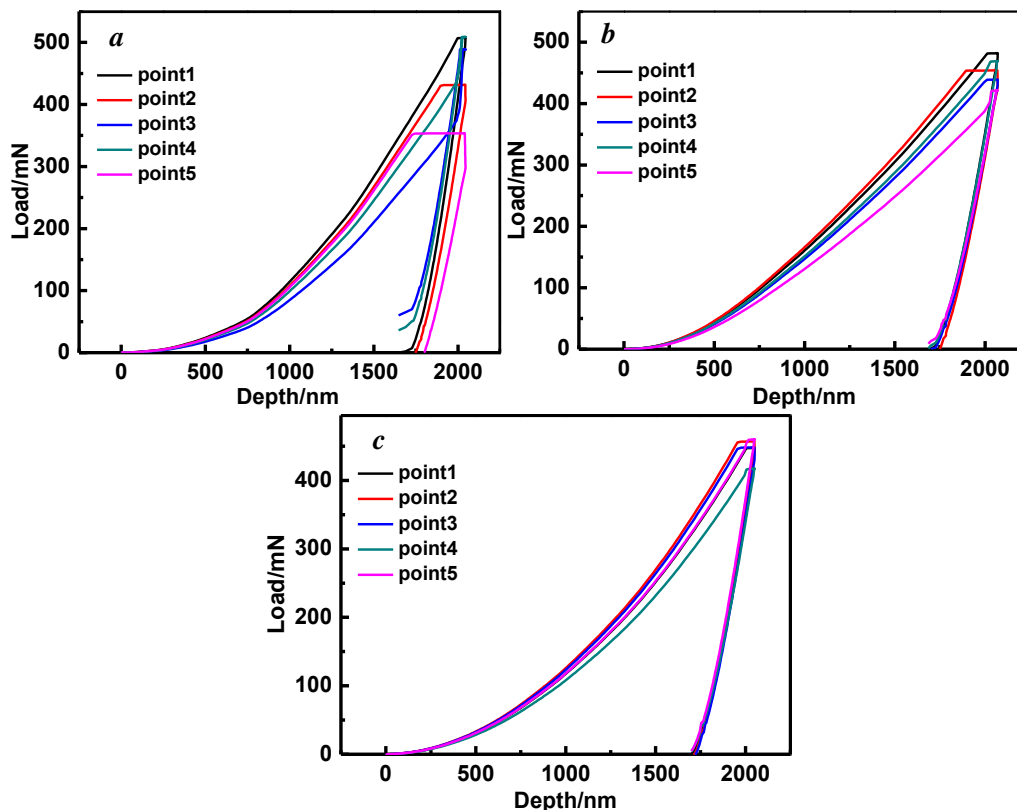
Figure 10. Nanoindentation curves of (a) Ni-Co alloy, (b) Ni-Co/ZrO$_2$ (5 g L^{-1}) and (c) Ni-Co/ZrO$_2$ (10 g L^{-1}) composite coatings.

3.4 Corrosion test

The corrosion behavior of Ni-Co alloy and Ni-Co/ZrO$_2$ composites was evaluated using the corrosion potential (E_{corr}) and corrosion current density (i_{corr}) after polarization of each coating. The potentiodynamic polarization curves of Ni-Co/ZrO$_2$ composite coatings prepared with 0, 5 and 10 g L^{-1} ZrO$_2$ in a 3.5 wt% NaCl solution were obtained as shown in Fig. 11, respectively. Table 4 illustrates the E_{corr} and i_{corr} values obtained by extrapolating the anodic and cathodic branches using the Tafel method. The Ni-Co/ZrO$_2$ composite coatings had better anti-resistance than Ni-Co alloy coatings. With the addition of ZrO$_2$ in the plating bath, the corrosion potential (E_{cor}) shifted positively, whereas the corrosion current density (i_{corr}) decreased significantly. Such a shift can be ascribed to the modification in grain size and crystal structure of the composite coatings and to the incorporated ZrO$_2$ that acted as physical barrier to the initiation and diffusion of corrosion, thereby improving the corrosion resistance of the Ni-Co/ZrO$_2$ composite coatings. The present result is in good agree with the research of E.

Beltowska-Lehman[23] who found increased anti-corrosion of Ni-W by the incorporation of ZrO_2 nanoparticles.
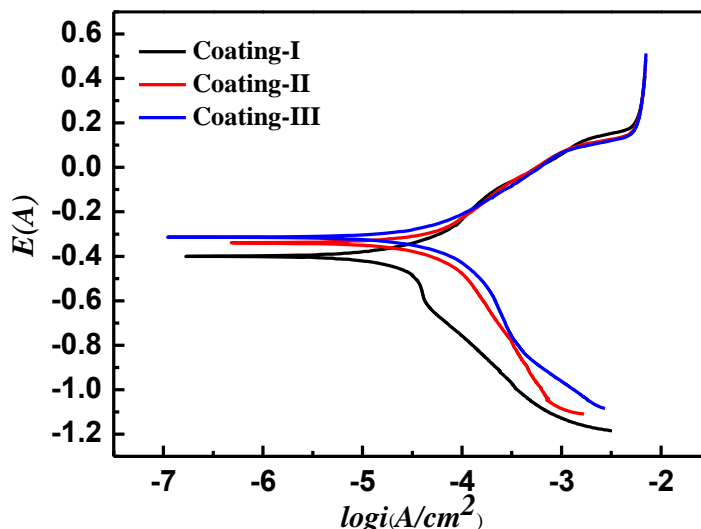
Figure 11. Potentiodynamic polarization curves of (I) Ni-Co alloy, (II) Ni-Co/ZrO_2 (5 g L^{-1}) and (III) Ni-Co/ZrO_2 (10 g L^{-1}) composite coatings in 3.5 wt% NaCl solution. T=55℃, pH=4.0, SR=20 mVs^{-1}.

Table 4. Summary of i_{corr} and E_{corr} of the Ni-Co alloy and Ni-Co/ZrO_2 composite coatings.

| Coating	E_{corr} vs. SCE (V)	i_{corr} ($\mu A/cm^2$)	Corrosion rate (mm/year)
I	-0.40	10.76	0.506
II	-0.34	8.29	0.338
III	-0.31	6.85	0.125

3.5 Friction test

Fig. 12 shows the friction coefficient versus the rotation time during the wear test. As shown in Fig. 12, the friction coefficient of the composite coating is obviously lower than that of the Ni-Co alloy and the copper matrix. The friction coefficient of Ni-Co alloy deposits fluctuates greatly, while averaging around 0.42, that of the Coating-II settles at 0.36 after 5 min of rotation, and that of the Coating-III tends to be more stable and is maintained at 0.32−0.34. During the initial few min of the friction test, the friction coefficients of the copper matrix and the Ni-Co alloy coating are small and roughly the same, this is because the rotating coupling region is mainly concentrated on uneven areas, therefore, the contact area of the sample and the coupling are small. Thus, the initial stage shows relatively low friction coefficients. The contact area of the sample and coupling increase gradually as the test proceeds. Simultaneously, the heat produced by friction gradually strengthens the adhesion between the friction pairs and the coating, and the friction coefficient also gradually increases. However, the coefficient of friction of Ni-Co/ZrO_2 composite coating fluctuates slightly. This is attributed to the ZrO_2 particles embedded in the composite coating that reduce the adhesion between the coating and the friction parts, thereby reducing the coefficient of friction of Ni-Co/ZrO_2 composite coatings. The friction coefficient

of the composite coating decreases as the ZrO_2 content in the plating solution increases, and the friction performance improves gradually, which is mainly attributed to the increase of the ZrO_2 particles in the composite coating.
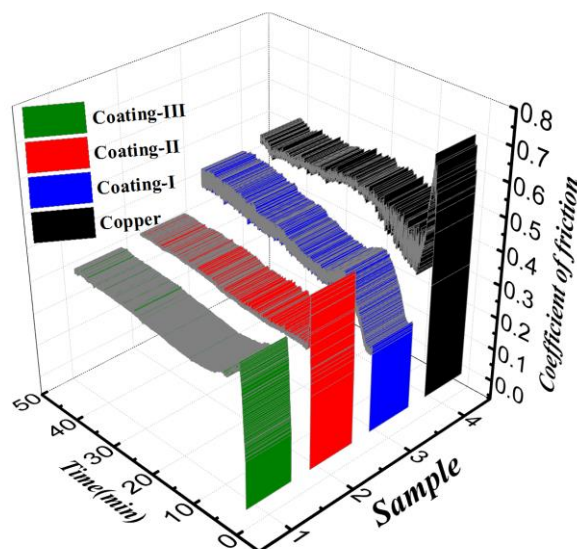
Figure 12. The friction coefficients of copper, (I) Ni-Co alloy, (II) Ni-Co/ZrO_2 (5 g L^{-1}) and (III) Ni-Co/ZrO_2 (10 g L^{-1}) composite coatings.
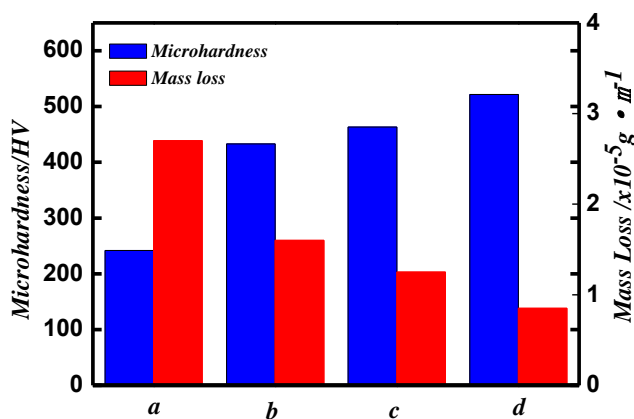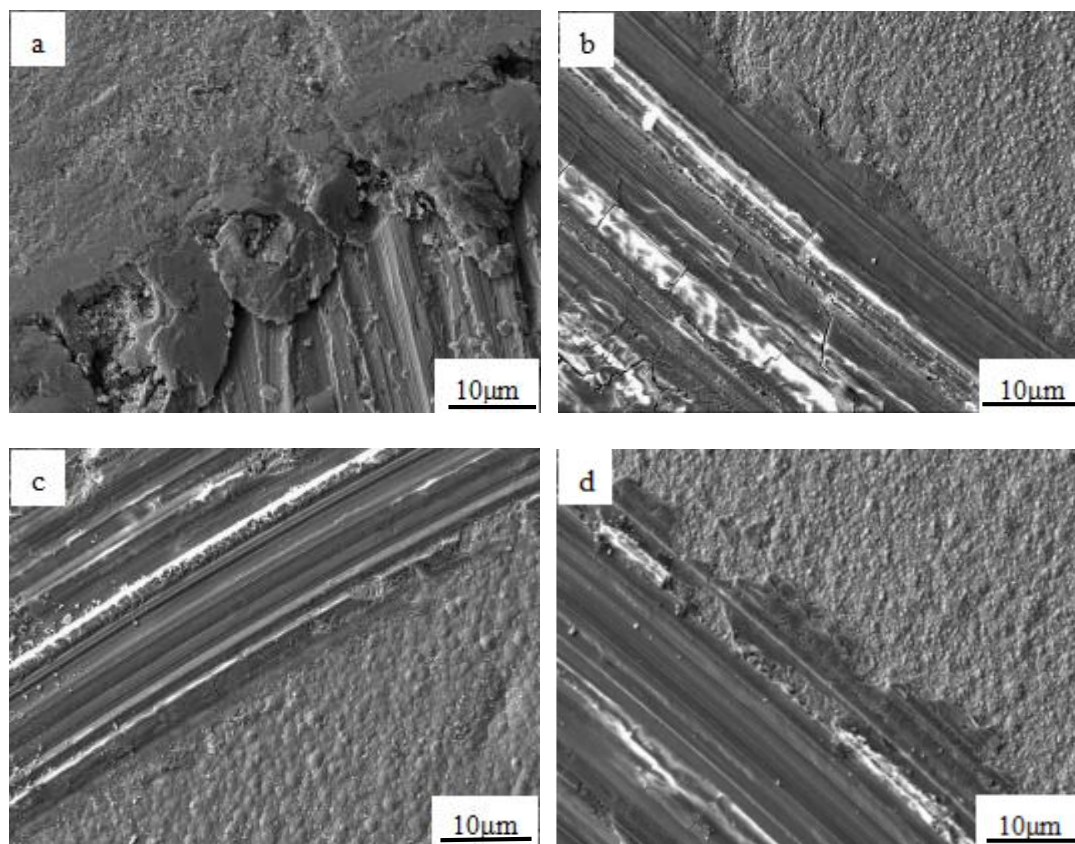

Figure 13. The wear mass loss and microhardness of copper, (I) Ni-Co alloy, (II) Ni-Co/ZrO_2 (5 g L^{-1}) and (III) Ni-Co/ZrO_2 (10 g L^{-1}) composite coatings.

The wear loss and average microhardness of the samples are presented in Fig. 13. The microhardness for the copper substrate, Coating-I, Coating-II and Coating-III are 241.74, 432.98, 463.18 and 521.6 HV, respectively, and the wear loss was 2.7×10^{-5}, 1.6×10^{-5}, 1.25×10^{-5} and 0.85×10^{-5} g·m^{-1}, respectively. As the microhardness of the coating increased, the wear loss gradually decreased; thus, the microhardness of the coating is inversely proportional to the wear loss. According to previous studies [24], when the size of the second phase particles embedded in a composite is below 100nm, a dispersion strengthening effect is exhibited inside the coating, improving the bearing capacity and deformation resistance of the coating and enhancing its wear resistance. SEM and XRD show a

significant grain refinement effect resulting from adding ZrO_2 particles to Ni-Co; the microhardness and anti-wear property of the Ni-Co/ZrO_2 composite coating were improved mainly due to two aspects: (1) grain-refining of the Ni-Co alloy metal matrix; (2) the dispersion strengthening effect of nanoparticles in the coating.

Fig. 14 shows the worn surface morphology of the copper matrix, Ni-Co alloy and Ni-Co/ZrO_2 composite coatings under a 400-g constant load. As seen in Fig. 14a, the wear mechanism of the copper matrix is adhesive, and the surface shows severe wear defects and plastic deformation accompanied by the accumulation of large debris. This is compatible with its lower microhardness, higher friction coefficient and shorter wear life. Fig. 14b shows there is a broad and deep grinding crack in the Ni-Co alloy coating, with obvious cracks and the accumulation of debris and plastic flow around the mark, indicating a composite wear mechanism of adhesive and abrasive wear. As shown in Figs. 14c and d, the grinding crack in the Ni-Co/ZrO_2 composite coating is narrow and shallow compared with that in the Ni-Co alloy coating. This is due to the supporting role of ZrO_2 particles as hard particles in the composite coating [25], avoiding adhesion between the ball and the coating surface. As shown by the small particles on the left side of Fig. 14c, the nanoparticles act as granular abrasives in wear, thus the wear mechanism of composite coatings is abrasive wear.

Figure 14. The wear morphology of copper, (I) Ni-Co alloy, (II) Ni-Co/ZrO_2 (5 g L^{-1}) and (III) Ni-Co/ZrO_2 (10 g L^{-1}) composite coatings.

The Ni-Co/ZrO_2 composite coating exhibits better wear resistance as compared to due Ni-Co alloy coating due to the following two reasons: on one hand, the cavitation phenomena caused by

ultrasound strengthened the mass transfer and diffusion, accelerated the charge transfer, and improved the cathodic current efficiency, leading to an increased amount of metal deposited on the surface that increased the coating thickness per unit time increased; on the other hand, the addition of ZrO_2 particles promoted heterogeneous nucleation and refined the grains of the Ni-Co alloy. When ZrO_2 was used in the form of second phase particles embedded in the metal matrix, due to the dispersion strengthening effect. The particles embedded in the metal matrix also impeded dislocation and lattice distortion. The combined action of these two aspects remarkably improved the wear resistance of the composite coating.

4. CONCLUSION

An ultrasonically electrodeposited ZrO_2-strengthened Ni-Co coating was prepared from an aminosulfonate bath, and the electrochemical behavior of Ni-Co/ZrO_2 composite deposition under an ultrasonic electric field as well as the effect of ZrO_2 on the microstructure and properties of coatings were investigated. The deposition behavior of Co^{2+} followed a 3D "nucleation/growth" mechanism, and the ZrO_2 nanoparticles can reduced the polarization of the system, causing the deposition potential to shift from -0.72 to -0.70 V. An $\approx25\%$ decrease in the coefficient of friction and wear indicated the improved tribological properties of the Ni-Co coating with 10 g L^{-1} ZrO_2. The incorporation of ZrO_2 improved the deposition of Ni-Co/ZrO_2 and the mechanical properties of the coating. Ultrasound can effectively promote the dispersion of nanoparticles in the electrolyte, resulting in the increase of the content of nanoparticles in the composite, and further improving the composite electrodeposition process and coating properties.

AUTHOR CONTRIBUTIONS
Y.W. conceived and designed the experiments; Z.L. and X.Z. performed the experiments; Z.L. analyzed the data; H.J. contributed reagents/materials/analysis tools; Y.W. wrote the paper.

DECLARATIONS OF INTEREST:
none

References

1. Z. Shafiee, M.E. Bahrololoom and B. Hashemi, *Mater. Design.*, 108 (2016) 19-26.
2. F.F. Xia, W.C. Jia, C.Y. Ma and J. Wang, *Ceram. Int.,* 44 (1) (2017) 766-773.
3. Z.P. Liang, Y.Y. Wang, H. Jin, X.Y. Zhou and X.L. Liu, *J. Mater. Eng.,* 46 (5) (2018) 112-119.
4. X. Liang, G. Gao, Y. Liu, T. Zhang and G Wu, *J. Alloys. Compd.,* 3 (2017) 67-73.
5. J.L.K Jayasingha, M.N. Kaumal, K.M.D.C. Jayathilaka, M.S. Gunewardene and D.P. Dissanayake, P*hysica. Status. Solidi.,* 214 (2017) 8.
6. T. He, Y. He, H. Li, Y. Fan, Q.B. Yang and Z. He, *J. Alloys. Compd.,* 743 (2018) 63-72.

7.   S.A. Ataie and A. Zakeri, *J. Alloys. Compd.,* 674 (2016) 315-322.
8.   I. Tudela, Y. Zhang, M. Pal, I. Kerr and A.J. Cobley, *Surf. Coat. Tech.,* 276 (2015) 89-105.
9.   E. García-Lecina, I. García-Urrutia, J.A. Díez, J. Fornell and E. Pellicer, *Electrochim. Acta.,* 114 (2013) 859-867.
10. W. Zhang, *Int. J. Electrochem. Sci.,* 13 (2018) 3486-3500.
11. S. Ranganatha, T.V. Venkatesha and K. Vathsala, *Surf. Coat. Tech.,* 208 (2012) 64-72.
12. K. Vathsala and T.V. Venkatesha, *Appl. Surf. Sci*., 257 (2011) 8929.
13. L.X. Song, Z. Zhang and J.Q. Zhang, *Acta. Metall. Sin-eng.,* 47 (2011) 123-128.
14. G. Wu, N. Li, D.L. Wang, D.R. Zhou, B.Q. Xu and Kurachi Mitsuo, *Mater. Chem. Phys.,* 87 (2004) 411-419.
15. F.F. Xia, H.B. Xu, C. Liu, J.W. Wang, J.J. Ding and C.H. Ma, *Appl. Surf. Sci.*, 271 (2013) 7-11.
16. L. Benea, *J. Appl. Electrochem.,* 39 (10) (2009) 1671-1681.
17. 17.N.Haghmoradi,C. Dehghanian and S. YariL, *J. Mater. Eng. Perform.,* 9 (2016) 1-10.
18. W. Hu, C. Tan, H. Cui, Y. Liu and Z. Zheng , *J. Cent. S. Univ. Technol.,* 17 (2010) 460-466.
19. S. Singh, M. Sribalaji, N.P. Wasekar, S. Joshi and G. Sundararajan, *Appl. Surf. Sci.,* 364 (2016) 264-272.
20. I. Brooks and U. Erb , *Scr. Mater.,* 44 (5) (2001) 853-858.
21. A. Hefnawy, N. Elkhoshkhany and A. Essam, *J. Alloys. Compd.,* 735 (2017) 600-606.
22. B. Lv, X.H. Wang, Z.F. Hu and B.S. Xu, *Rare. Metal. Mat. Eng.,* 2 (2017) 555-560.
23. E. Beltowska-Lehmana, A. Bigosa, P. Indykab, A. Chojnackaa, A. Drewienkiewiczc, S. Zimowskid, M. Kotd and M.J. Szczerbaa, *J. Electroanal. Chem.,* 813 (2018) 39-51.
24. N. Li and C.H. Gao, *Mater. Sci. Tech-lond.,* 19 (2011) 104-109.
25. G.Z. Ma, B.S. Xu and H.D. Wang, *J.Mat. Eng., 24.* (2010) 66-71.